Mid-infrared laser diodes epitaxially grown on on-axis (001) silicon

M. Rio Calvo, Laura Monge-Bartolomé, M. Bahriz, Guilhem Boissier, Laurent Cerutti, Jean-Baptiste Rodriguez, Eric Tournié

optica

Mid-infrared laser diodes epitaxially grown on on-axis (001) silicon

Marta Rio Calvo,† Laura Monge Bartolomé,† Michaël Bahriz, Guilhem Boissier, Laurent Cerutti, Jean-Baptiste Rodriguez, and Eric Tournié*

IES, University of Montpellier, CNRS, F-34000 Montpellier, France
**Corresponding author: eric.tournie@umontpellier.fr*

Received 17 January 2020; revised 20 February 2020; accepted 25 February 2020 (Doc. ID 388383); published 26 March 2020

The direct epitaxial growth of III-V semiconductor lasers on standard, CMOS-compatible, on-axis (001) Si substrates is actively sought for the realization of active photonic integrated circuits. Here we report on the first mid-infrared semiconductor laser epitaxially grown on on-axis Si substrates, i.e., compatible with industry standards. Furthermore, these GaSb-based laser diodes demonstrate low threshold current density, low optical losses, high temperature operation, and high characteristic temperatures. These results represent a breakthrough toward the integration of semiconductor laser sources on Si for smart sensors.

https://doi.org/10.1364/OPTICA.388383

The short-wave portion of the mid-infrared (mid-IR) electromagnetic spectrum (SWIR) covers the 1.6–3 μm range. It includes transparence windows of the atmosphere as well as absorption lines for many molecules [1] that are important for medical and industrial applications, as well as for environmental monitoring. GaSb-based laser diodes (LDs) have progressively emerged as the unique semiconductor laser technology able to fully cover this wavelength range [2,3], and they have allowed high-sensitivity optical gas sensing [4–6]. Still, up to now these sensors are rather bulky and expensive, largely due to the fact that they rely on discrete devices. This situation hinders their widescale deployment, in spite of a strong societal demand.

Silicon photonics offers the prospect of building inexpensive, compact, integrated sensors in the SWIR based on mature CMOS processes because silicon, Si_3N_4, and SiO_2 are transparent [7]. A large portfolio of passive photonic elements has indeed been demonstrated in this wavelength range [8,9]. This is in marked contrast to the situation at longer wavelengths where interband-cascade lasers (ICLs) or quantum-cascade lasers (QCLs) operate, which requires complex integration schemes [10,11] due to the SiO_2 or Si absorption [7].

The point that remains to be unlocked in order to achieve compact mid-IR sensors is the large-scale, cost-effective integration of III-V semiconductor lasers. Although most integration schemes until now have relied on heterogeneous bonding [10–13], there is increasing evidence that the direct epitaxial growth of the III-V semiconductor laser heterostructure on Si should outperform them, provided on-axis, CMOS-compatible (001)-oriented Si substrates can be used [14]. This last integration strategy, however, is challenged by the conjunction of large thermal, lattice, and polarity mismatches between the Si substrate and III-V materials [15]. In particular, the polarity mismatch easily gives rise to planar defects, the antiphase boundaries (APBs), that act as shorts in devices [16]. Ways to circumvent this issue have been established in the last few years, which notably led to the early demonstration of efficient InAs/GaAs quantum dot lasers (QDLs) emitting near 1.3 μm grown on on-axis Si substrates [17–19]. These achievements relied on a two-step strategy where either GaAs on patterned Si [17], GaAs on planar Si [18], or GaP on planar Si [19] templates were first prepared by metal-organic vapor phase epitaxy (MOVPE) before being transferred to another laboratory where the laser heterostructures were grown by molecular-beam epitaxy (MBE). On the other hand, laser diodes in the InP technology for emission near 1.5 μm have also been reported by an all-MOVPE approach, but they relied either on very thick (∼13 μm) buffer layers [20] or on patterned Si substrates [21,22], both of which are marginally compatible with industry standards. Finally, it has been recently demonstrated that by further optimizing the III-V-on-Si MBE growth, high-performance InAs/GaAs QDLs grown in a single all-MBE run on planar, on-axis Si could be achieved [23,24].

In contrast to the wealth of publications available in the data- and telecommunication wavelength ranges [25], very few works have reported on the epitaxial integration of mid-IR laser sources. GaSb-based LDs [26] and QCLs [27] and InP-based QCLs [28] have been previously demonstrated, but all of them were grown on large offcut (≥6°) Si substrates, not compatible with industry standards. In this Letter we report on the first—to the best of our knowledge—mid-IR semiconductor laser epitaxially grown on an on-axis, CMOS-compatible, Si substrate.

The whole epitaxial stack is depicted in Fig. 1. The core of the laser heterostructure is typical for GaSb-based LDs emitting near 2.3 μm [2,3], a wavelength where, among other greenhouse gases, CH_4 and NH_3 exhibit strong absorption lines [1]. The active zone is made of two $Ga_{0.67}In_{0.33}As_{0.08}Sb_{0.88}$ quantum wells (QWs) confined by $Al_{0.25}Ga_{0.75}As_{0.02}Sb_{0.98}$ barrier layers. This ensemble is embedded in an $Al_{0.25}Ga_{0.75}As_{0.02}Sb_{0.98}$ waveguide, itself clad by $Al_{0.9}Ga_{0.1}As_{0.07}Sb_{0.93}$ layers [Supplement 1]. All $Al_xGa_{1-x}As_ySb_{1-y}$ layers are matched, while the $Ga_{0.67}In_{0.33}As_{0.12}Sb_{0.88}$ QWs are mismatched by 1.5% with

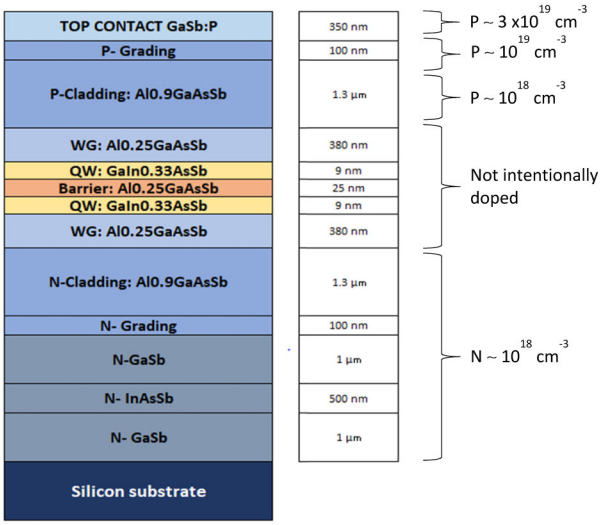

Fig. 1. Design of the laser heterostructure.

respect to the GaSb lattice parameter. The laser structure was grown by solid-source MBE on a (001)-oriented Si substrate exhibiting a residual miscut of ∼0.5°. Prior to growth the Si substrate was annealed at 1000°C for 10 min before the growth was initiated at low temperature (∼400°C). After 50 nm GaSb growth, the substrate temperature was raised to 500°C for completing a 1 µm thick GaSb buffer layer. Then the temperature was set at 470°C for growing an *n*-type, 500 nm thick $InAs_{0.92}Sb_{0.08}$ layer, an additional 1 µm thick *n*-type GaSb buffer layer, and the laser heterostructure. The $InAs_{0.92}Sb_{0.08}$ layer serves as both a marker during LD processing and the back-contact layer to the LDs. No dislocation filtering layer was inserted in the buffer layers.

Atomic-force microscopy (AFM) images of the surface revealed the absence of emerging APBs [Supplement 1]. This remarkable result is ascribed to the high-temperature preparation of the Si substrate and the two-temperature growth of the buffer layer. We show in Fig. 2(a) the high-resolution x-ray diffraction (HRXRD) curve taken from the sample. The occurrence of a single peak at the position of the GaSb diffraction angle confirms the lattice matching of the $Al_xGa_{1-x}As_ySb_{1-y}$ layers. The position of this peak indicates full relaxation of the GaSb-based heterostructure with respect to the Si substrate. Figure 2(b) shows a zoom around the GaSb peak together with the simulated pattern of the laser stack using the parameters of Fig. 1 and assuming that the active zone (A.Z.) is fully strained with respect to GaSb. The excellent agreement between simulated and experimental curves, together with well-pronounced and contrasted A.Z. features, confirm the assumption of strained QWs with respect to GaSb and that the QW–barrier layer interfaces are well defined in spite of the 12% lattice mismatch between GaSb and Si. An upper bound of 8.5×10^7 cm^{-2} threading dislocation density is estimated from preliminary transmission electron microscopy investigations [Supplement 1].

Ridge LDs were processed using standard photolithography and inductively coupled plasma reactive ion etching. The ridges were 5, 8, 10, or 100 µm wide. Electrical insulation and protection of the etched sidewalls were obtained using Si_3N_4 deposited by plasma-enhanced chemical vapor deposition. Both *p* and *n* contacts were taken on the epitaxial structure. The *p* contact was taken on the top ridge, while the *n* contact was taken on the

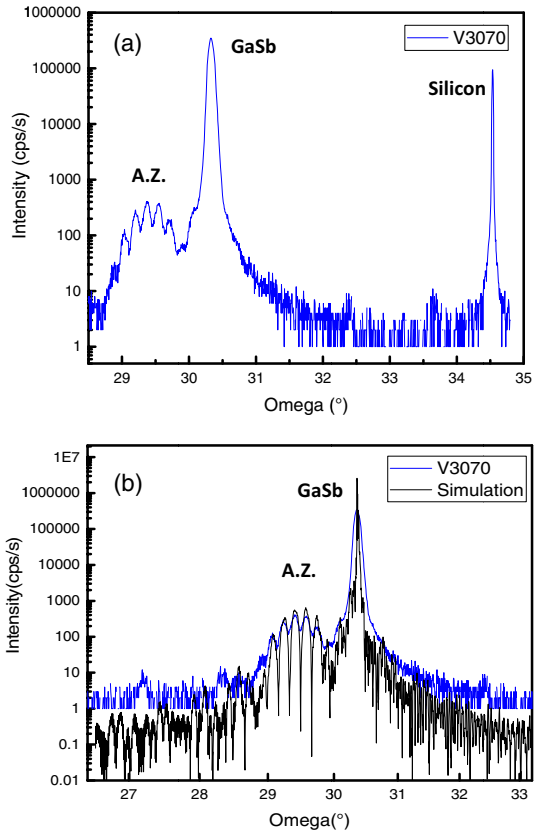

Fig. 2. (a) HRXRD curve taken from the heterostructure, (b) HRXRD curve around the GaSb peak (blue curve), together with the simulated pattern (black curve), assuming a fully strained active zone (A.Z.).

$InAs_{0.92}Sb_{0.08}$ layer located within the buffer layer stack. This geometry avoids driving the current through the highly defective III-V/Si interface and ensures higher LD performance [25]. Ti–Au and AuGeNi were used as contact metals for the *p*- and *n*-type contacts, respectively. Laser cavities of various length between 1 and 3 mm were formed by cleaving laser bars after substrate thinning. No optical treatment was applied to the facets. The laser bars were then soldered substrate-side-down on Cu heat sinks for being tested on a probe station.

Broad-area LDs with 100 µm wide ridges and various cavity length were first tested at room temperature under pulsed operation to access the threshold current density of the laser structure. The light-current-voltage (L-I-V) characteristics of these LDs are plotted in Fig. 3. The diode behavior of the devices confirms the absence of APBs crossing the *p-i-n* junction. The turn-on voltage of all LDs is around 0.6–1 V, which is expected for an active zone with such a bandgap, and it is comparable to what is measured with LDs grown on the native GaSb substrate [2,3]. The threshold current density is around 400−500 $A.cm^{-2}$ for all LDs, excellent values for QW LDs grown on Si and much better than on off-axis Si [26]. Still, these thresholds remain higher than those of similar LDs grown on GaSb [2,3] and those of GaAs QDLs emitting near 1.3 µm grown on on-axis Si [17–19,23,24], the best semiconductor lasers on Si to date. They are, however, notably lower than those of InP-based LDs emitting near 1.5 µm grown on on-axis Si [20–22].

Next the narrow-ridge LDs have been characterized in the continuous-wave (cw) regime at room temperature and above. We

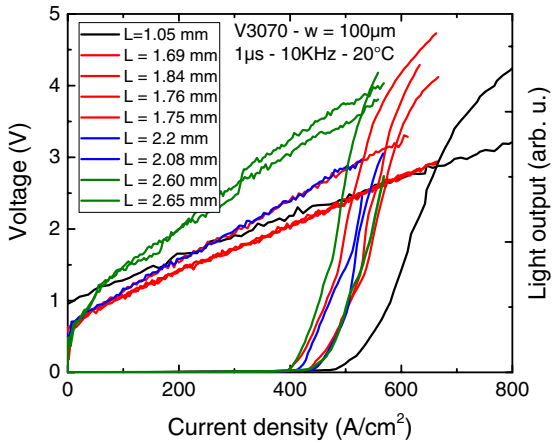

Fig. 3. L-I-V curves taken at room temperature from broad-area LDs with a ridge width of 100 µm and various cavity lengths.

show in Fig. 4 the L-I-V curves taken at 20°C from a series of LDs with a ridge width of 8 µm and various cavity lengths. The turn-on voltage is around 0.7–1 V, and the series resistance is in the 3–6 Ω range, comparable to that of LDs grown on offcut Si substrates [26]. The threshold current ranges from 75 to 200 mA, depending on the cavity length. The output power per uncoated facet reaches the 10 mW range.

The slope efficiency (per facet) varies from 0.09 to 0.16 W/A, depending on the cavity length. The external quantum efficiencies η_d (related to both facets) have been extracted from Fig. 4, and their inverse values are plotted against the cavity length in the inset of Fig. 4 and fitted using Eq. (1) [29], where η_d and η_i are the external differential and internal quantum efficiencies, respectively, R is the power reflectivity of the facets, α_i represents the internal losses, and L is the cavity length:

$$\frac{1}{\eta_d}=\frac{1}{\eta_i}+\frac{\alpha_i}{\eta_i \ln\left(R^{-1}\right)}L. \tag{1}$$

The intercept gives $\eta_i = 34\%$ for the internal quantum efficiency. Assuming $R = 0.3$ for the power reflectivity of the cleaved facets [29], the slope of the η_d^{-1} versus L fit allows extraction of internal loss values as low as $\alpha_i \sim 2\ \mathrm{cm}^{-1}$. Similar values for η_i and α_i, are obtained from the series of LDs with ridge widths of 5 and 10 µm [Supplement 1].

Next we show in Fig. 5 the laser spectra taken at 20°C under two different cw drive currents from a LD with an 8 µm ridge width and 1 mm cavity length. The emission is close to 2.3 µm, as expected from the heterostructure design. It shifts by about 4 nm when the drive current is increased from 110 to 150 mA, corresponding to a 0.1 nm/mA shift rate. This is mainly due to the active zone heating upon cw current injection. From the variation of the bandgap versus temperature [30], we estimate that the temperature of the active zone increases by about 20 K when the current increases from 110 to 150 mA. Such a wavelength tunability is necessary to perform spectroscopy sensing.

Finally, we show in Fig. 6 the L-I-V curves taken under cw operation between 20°C and 80°C—limited by our experimental setup—from a LD with an 8 µm ridge width and 1.75 mm cavity length. The turn-on voltage varies between ~ 0.9 and ~ 0.7 V in this temperature range due to the bandgap variation. The series resistance varies marginally and is ~ 4 Ω. The threshold current increases from 125 mA at 20°C to 200 mA at 80°C. It is noticeable that there is no hint of thermal rollover, even at 80°C. The inset in Fig. 6 shows the semi-logarithmic plots of the threshold current and of the external differential quantum efficiency as a function of the temperature. The slopes allow extraction of the so-called T_0 and T_1 characteristic temperatures, which represent the sensitivity of these parameters to the device temperature. The values obtained from Fig. 6 are $T_0 = 123$ K and $T_1 = 234$ K, comparable to those obtained with LDs grown on GaSb [Supplement 1].

The properties of these LDs grown on on-axis Si are much better than those of their counterparts grown on 6°-offcut Si substrates [26], and one can expect that introducing dislocation filtering layers should bring the threshold current density even closer to that of LDs grown on native GaSb substrates. We ascribe this step forward to several origins. First, to a much higher material quality due to the absence of APBs and to the on-axis growth plane. Indeed, the concomitant presence of APBs and substrate misorientation leads to severe step bunching and complex defect microstructure [31]. In addition, since our original work [26] we have totally revised the LD fabrication steps, and in particular have introduced ICP etching instead of wet etching. Finally, on-axis wafers cleave more readily than highly miscut ones, resulting in better LD facet quality. Nevertheless, more work is needed on both

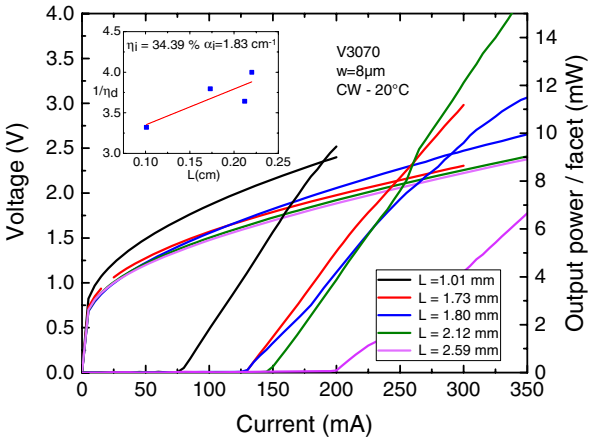

Fig. 4. L-I-V curves taken at room temperature from LDs with a ridge width of 8 µm and various cavity lengths. The inset shows the evolution of $1/\eta_d$ (double-facet values) as a function of the cavity length.

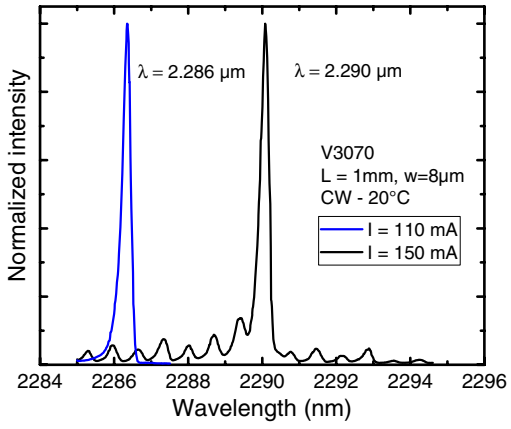

Fig. 5. Laser spectra taken under 110 mA and 150 mA cw drive current for a LD with an 8 µm wide ridge and a 1 mm long cavity. The measurement setup temperature was 20°C.

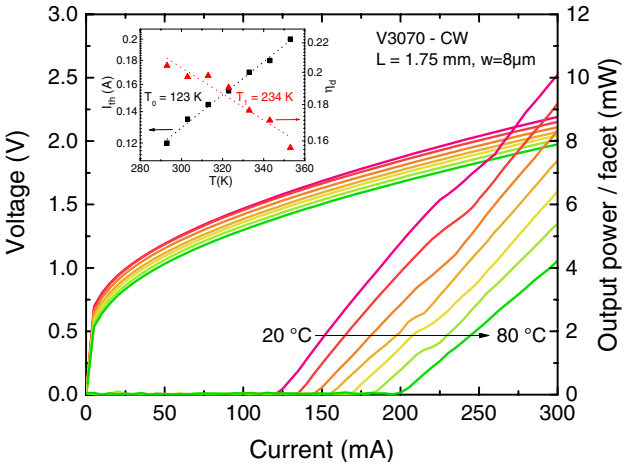

Fig. 6. L-I-V curves taken under cw operation between 20°C and 80°C from a LD with an 8 μm ridge width and 1.75 mm cavity length. The inset shows the semi-logarithmic variation of I_{th} and η_d with temperature.

the fundamental material science and laser physics points of view to fully unravel the origin of the device's performance.

In conclusion, we have reported high-performance GaSb-based QW LDs epitaxially grown on an on-axis (001) Si substrate that operate under cw operation at high temperature. This epitaxial approach can be applied to any GaSb-based optoelectronic devices, including ICLs, QCLs, and photodetectors, which represents a breakthrough in view of the fabrication of fully integrated mid-IR sensors.

Funding. Agence Nationale de la Recherche (ANR-11-EQPX-0016); H2020 LEIT Information and Communication Technologies (780240).

Acknowledgment. Dr. G. Patriarche (C2N, CNRS, U. Paris-Saclay) for preliminary transmission electron microscopy experiments.

Disclosures. The authors declare no conflicts of interest.

See Supplement 1 for supporting content.

†These authors contributed equally to this work.

REFERENCES AND NOTES

1. L. S. Rothman and I. E. Gordon, AIP Conf. Proc. **1545**, 223 (2013).
2. G. Belenky, L. Shterengas, M. V. Kisin, and T. Hosoda, *Semiconductor Lasers: Fundamentals and Applications*, A. N. Baranov and E. Tournié, eds. (Woodhead Publishing, 2013), p. 441.
3. L. Cerutti, A. A. Vicet, and E. Tournié, *Mid-Infrared Optoelectronics: Materials, Devices, Applications*, E. Tournié and L. Cerutti, eds. (Elsevier, Woodhead Publishing, 2019), p. 91.
4. T. Bleuel, M. Brockhaus, J. Koeth, J. Hofmann, R. Werner, and A. Forchel, Proc. SPIE **3858**, 119 (1999).
5. A. Vizbaras, E. Dvinelis, A. Trinkunas, I. Simonyte, M. Greibus, M. Kausylas, T. Zukauskas, R. Songaila, and K. Vizbaras, Proc. SPIE **9081**, 90810P (2014).
6. T. Milde, M. Hoppe, H. Tatenguem, M. Honsberg, M. Mordmuller, J. O'Gorman, W. Schade, and J. Sacher, Proc. SPIE **10553**, 105530C (2018).
7. R. Soref, Nat. Photonics **4**, 495 (2010).
8. G. Roelkens, U. D. Dave, A. Gassenq, N. Hattasan, C. Hu, B. Kuyken, F. Leo, A. Malik, M. Muneeb, E. M. P. Ryckeboer, D. Sanchez, S. Uvin, R. Wang, Z. Hens, R. Baets, Y. Shimura, F. Gencarelli, B. Vincent, R. Loo, J. Van Campenhout, L. Cerutti, J. B. Rodriguez, E. Tournié, X. Chen, and M. Nedeljkovic, IEEE J. Sel. Top. Quantum Electron. **20**, 8201511 (2014).
9. L. Tombez, E. J. Zhang, J. S. Orcutt, S. Kamlapurkar, and W. M. J. Green, Optica **4**, 1322 (2017).
10. A. Spott, J. Peters, M. L. Davenport, E. J. Stanton, C. D. Merritt, W. W. Bewley, I. Vurgaftman, C. S. Kim, J. R. Meyer, J. Kirch, L. J. Mawst, D. Botez, and J. E. Bowers, Optica **3**, 545 (2016).
11. A. Spott, E. J. Stanton, A. Torres, M. L. Davenport, C. L. Canedy, I. Vurgaftman, M. Kim, C. S. Kim, C. D. Merritt, W. W. Bewley, J. R. Meyer, and J. E. Bowers, Optica **5**, 996 (2018).
12. N. Hattasan, L. Cerutti, J. B. Rodriguez, E. Tournié, D. Van Thourout, and G. Roelkens, Proc. SPIE **7945**, 79451K (2011).
13. R. Wang, S. Sprengel, A. Vasiliev, G. Boehm, J. Van Campenhout, G. Lepage, P. Verheyen, R. Baets, M.-C. Amann, and G. Roelkens, Photon. Res. **6**, 858 (2018).
14. A. Y. Liu and J. E. Bowers, IEEE J. Select. Top. Quant. Electron. **24**, 6000412 (2018).
15. H. Kroemer, J. Cryst. Growth **81**, 193 (1987).
16. B. Galiana, I. Rey-Stolle, I. Beinik, C. Algora, C. Teichert, J. M. Molina-Aldareguia, and P. Tejedor, Sol. Energy Mater. Sol. Cells **95**, 1949 (2011).
17. J. Norman, M. J. Kennedy, J. Selvidge, Q. Li, Y. Wan, A. Y. Liu, P. G. Callahan, M. P. Echlin, T. M. Pollock, K. M. Lau, A. C. Gossard, and J. E. Bowers, Opt. Express **25**, 3927 (2017).
18. S. Chen, M. Liao, M. Tang, J. Wu, M. Martin, T. Baron, A. Seeds, and H. Liu, Opt. Express **25**, 4632 (2017).
19. A. Y. Liu, J. Peters, X. Huang, D. Jung, J. Norman, M. L. Lee, A. C. Gossard, and J. E. Bowers, Opt. Lett. **42**, 338 (2017).
20. M. Sugo, H. Mori, Y. Sakai, and Y. Ltoh, Appl. Phys. Lett. **60**, 472 (1992).
21. S. Zhu, B. Shi, Q. Li, and K. M. Lau, Appl. Phys. Lett. **113**, 221103 (2018).
22. B. Shi, H. Zhao, L. Wang, B. Song, S. Tommaso, S. Brunelli, and J. Klamkin, Optica **6**, 1507 (2019).
23. J. Kwoen, B. Jang, J. Lee, T. Kageyama, K. Watanabe, and Y. Arakawa, Opt. Express **26**, 11568 (2018).
24. J. Kwoen, B. Jang, K. Watanabe, and Y. Arakawa, Opt. Express **27**, 2681 (2019).
25. See, e.g., Semicond. Semimetals Vol. 99 (2018) and Vol. 101 (2019).
26. J. R. Reboul, L. Cerutti, J. B. Rodriguez, P. Grech, and E. Tournié, Appl. Phys. Lett. **99**, 121113 (2011).
27. H. Nguyen-Van, A. N. Baranov, Z. Loghmari, L. Cerutti, J.-B. Rodriguez, J. Tournet, G. Narcy, G. Boissier, G. Patriarche, M. Bahriz, E. Tournié, and R. Teissier, Sci. Rep. **8**, 7206 (2018).
28. R. Go, H. Krysiak, M. Fetters, P. Figueiredo, M. Suttinger, X. M. Fang, A. Eisenbach, J. M. Fastenau, D. Lubyshev, A. W. K. Liu, N. G. Huy, A. O. Morgan, S. A. Edwards, M. J. Furlong, and A. Lyakh, Opt. Express **26**, 22389 (2018).
29. See, e.g., L. A. Coldren, S. W. Corzine, and M. L. Masanovic, Diode Lasers and Photonic Integrated Circuits (Wiley, 2012).
30. C.-L. Lin, Y.-K. Su, J.-R. Chang, S.-M. Chen, W.-L. Li, and D.-H. Jaw, Jpn. J. Appl. Phys. **39**, L400 (2000).
31. M. Niehle, J.-B. Rodriguez, L. Cerutti, E. Tournié, and A. Trampert, Phys. Status Solidi (RRL) **13**, 1900290 (2019).